ACSNANO

www.acsnano.org

ARTICLE

Partial Leidenfrost Evaporation-Assisted Ultrasensitive Surface-Enhanced Raman Spectroscopy in a Janus Water Droplet on Hierarchical Plasmonic Micro-/Nanostructures

Junyeob Song,[§] Weifeng Cheng,[§] Meitong Nie, Xukun He, Wonil Nam, Jiangtao Cheng,* and Wei Zhou*

Cite This: *ACS Nano* 2020, 14, 9521−9531

Read Online

ACCESS | Metrics & More | Article Recommendations | Supporting Information

ABSTRACT: The conventional methods of creating superhydrophobic surface-enhanced Raman spectroscopy (SERS) devices are by conformally coating a nanolayer of hydrophobic materials on micro-/nanostructured plasmonic substrates. However, the hydrophobic coating may partially block hot spots and therefore compromise Raman signals of analytes. In this paper, we report a partial Leidenfrost evaporation-assisted approach for ultrasensitive SERS detection of low-concentration analytes in water droplets on hierarchical plasmonic micro-/nanostructures, which are fabricated by integrating nanolaminated metal nanoantennas on carbon nanotube (CNT)-decorated Si micropillar arrays. In comparison with natural evaporation, partial Leidenfrost-assisted evaporation on the hierarchical surfaces can provide a levitating force to maintain the water-based analyte droplet in the Cassie−Wenzel hybrid state, *i.e.*, a Janus droplet. By overcoming the diffusion limit in SERS measurements, the continuous shrinking circumferential rim of the droplet, which is in the Cassie state, toward the pinned central region of the droplet, which is in the Wenzel state, results in a fast concentration of dilute analyte molecules on a significantly reduced footprint within several minutes. Here, we demonstrate that a partial Leidenfrost droplet on the hierarchical plasmonic surfaces can reduce the final deposition footprint of analytes by 3−4 orders of magnitude and enable SERS detection of nanomolar analytes (10^{-9} M) in an aqueous solution. In particular, this type of hierarchical plasmonic surface has densely packed plasmonic hot spots with SERS enhancement factors (EFs) exceeding 10^7. Partial Leidenfrost evaporation-assisted SERS sensing on hierarchical plasmonic micro-/nanostructures provides a fast and ultrasensitive biochemical detection strategy without the need for additional surface modifications and chemical treatments.

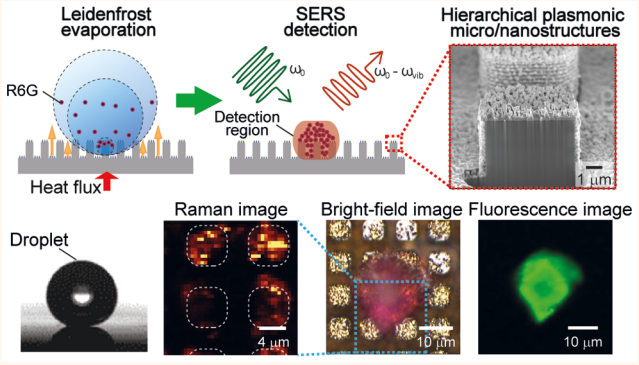

KEYWORDS: *surface-enhanced Raman scattering, hierarchical plasmonic micro-/nanostructures, Leidenfrost evaporation, ultrasensitive biochemical detection, surface wettability control by heating*

During the past several decades, surface-enhanced Raman spectroscopy (SERS) has been developed as an ultrasensitive molecular detection technique for (bio)chemical sensing and analyses.[1−3] By increasing both the laser excitation and the inelastic Raman scattering rates from analyte molecules in hot spots of intense optical fields, plasmonic nanostructures can achieve a SERS enhancement factor (EF) above 10^7.[4−6] In particular, metal−insulator−metal (MIM) nanocavities with sub-10 nm plasmonic nanogaps can foster gap surface plasmon modes[7,8] and allow extremely hot spots with SERS EFs up to 10^{10}.[9] A recent trend in SERS research is to achieve a fast and high-sensitivity detection of analytes at ultralow concentrations for applications ranging from point-of-care biomedical diagnoses, food and water quality analyses, to environmental monitoring.[3,10−12] However,

Received: May 21, 2020
Accepted: June 26, 2020
Published: June 26, 2020

https://dx.doi.org/10.1021/acsnano.0c04239
ACS Nano 2020, 14, 9521−9531

the diffusion-limited transport processes make it very challenging to effectively deliver analytes of subnanomolar-level low concentrations into sparse sub-10 nm-scale hot spots on the SERS substrates within a relatively short detection time window.[13,14] Toward SERS detection of ultralow-concentration analyte solutions beyond the diffusion limit, a commonly adopted method is to develop superhydrophobic SERS substrates with a high contact angle (>150°) of analyte droplets during natural evaporation and to reduce the analyte deposition area (~50 × 50 μm^2).[15] Superhydrophobic SERS substrates have been created by coating hydrophobic nanolayers of Teflon-like fluoropolymer or surface-assembled perfluoro-monolayer on three-dimensional (3D) nanostructured plasmonic substrates, such as Ag nanostructures on Si micropillar arrays,[15,16] self-assembled Ag-nanocube arrays,[17,18] Ag microbowl/nanoparticle arrays, and 3D forestlike Ag nanodendrites,[19] *etc.* Despite the advantage of straightforward design and fabrication, superhydrophobic SERS substrates composed of plasmonic nanostructures with hydrophobic coatings still have some unsolved issues including (1) the partial blocking of hot spots by the hydrophobic nanolayers;[20] (2) the spectral Raman band interference between the analytes and the hydrophobic coating at hot spots; and (3) limited reusability due to the laser-induced degradation of the hydrophobic coating that is exacerbated by plasmonic photochemical/photothermal effects. One solution to these issues is to introduce predefined micrometer-scale islands of superhydrophilic plasmonic nanostructures with fresh SERS hotspots on the superhydrophobic SERS substrates using lithography patterning techniques,[21] which requests complex microfabrication and surface treatments. Recent studies show that Ag-based 3D hierarchical plasmonic nanostructures without any hydrophobic coatings can form a high-adhesive quasi-superhydrophobic surface after exposure to the atmosphere,[22] allowing them to serve as a quasi-superhydrophobic SERS substrate for low-concentration analyte detection.[22−26] However, Ag-based high-adhesive quasi-superhydrophobic SERS substrates have a large contact angle hysteresis so that analyte droplets can easily get pinned thereon during natural evaporation, leading to a relatively large analyte deposition footprint (~1 mm^2).[22,24] Alternatively, by mixing discrete plasmonic nanoparticles with analyte solutions, ultrasensitive SERS detection of ultralow-concentration analytes can be achieved by drying the droplet of mixture solutions on the hydrophobic surfaces, which can result in a highly concentrated mixture of plasmonic nanoparticles and analyte molecules within a small deposition area for SERS measurements.[27−29] However, SERS detection techniques based on the analyte−nanoparticle mixtures suffer from some disadvantages such as poor reproducibility for quantitative analysis, extra sample preparation steps, and low scalability for multiplexed measurements of different analyte solutions.

In this work, we report an ultrasensitive SERS detection strategy based on a partial Leidenfrost manipulation of analyte droplets on hierarchical plasmonic micro-/nanostructures without any hydrophobic surface coatings (Figure 1). In general, the Leidenfrost effect means that a liquid droplet sitting on a superheated surface can be levitated by a thin layer of self-evaporated vapor underneath, which also functions as a thermal barrier to prevent the droplet from boiling.[30,31] During the conventional Leidenfrost evaporation, the whole droplet hovering over the vapor layer can be easily dislodged from the surface due to the potentially strong vapor convection therein.

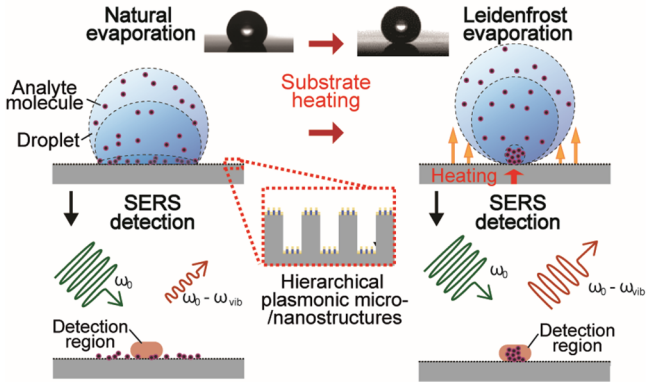

Figure 1. Schematic of partial Leidenfrost evaporation-assisted SERS detection of low-concentration analyte molecules in a Janus water droplet on hierarchical plasmonic micro-/nanostructures.

Nevertheless, hierarchical plasmonic micro-/nanostructures are adopted by us for Leidenfrost evaporation-assisted concentration of dilute analytes in a water droplet and ultrasensitive SERS detection. Without the hydrophobic coating, a liquid droplet on the hierarchical plasmonic micro-/nanostructures is initially in the Wenzel state,[32] featured with a relatively small contact angle of ~140° and an otherwise large final deposition area of ~4 mm^2. By carefully increasing the substrate temperature from the room temperature beyond a threshold temperature of ~120 °C, a layer of the evaporated vapor would first form along the circumferential rim of the droplet, which means the circumferential region switches to the Cassie state[32] with a relatively larger contact angle of ~170°. By meticulously moderating the substrate heating process, we demonstrate that it is possible to levitate up only the circumferential region of a liquid droplet, *i.e.*, in the Cassie state, while pinning the central region of the droplet on the hierarchical plasmonic micro-/nanostructures, *i.e.*, in the Wenzel state. Throughout such a dynamically tuned partial Leidenfrost evaporation process, the analyte droplet maintained in the Cassie−Wenzel hybrid state (Figure S1, Supporting Information) can continuously shrink toward the pinned central spot, leading to a minimized analyte deposition footprint for ultrafast and ultrasensitive SERS detection without the need for any additional surface treatments. This design of the micro-/nanostructured surfaces (1) provides a plethora of plasmonic nanostructures as intrinsic SERS hot spots; (2) provides micro-/nanopillar structures to reduce the threshold temperature for partial Leidenfrost evaporation of the analyte droplet especially at the circumferential rim; and (3) provides a pinning force at the bottom center of the analyte droplet, which is still in the Wenzel state, to avoid the dislodgement of the droplet during partial Leidenfrost evaporation and hence concentrate the analyte molecules at the prescribed position for reliable SERS measurements. As illustrated in Figure 1, compared to natural evaporation, partial Leidenfrost evaporation of analyte droplets on the hierarchical plasmonic micro-/nanostructures can significantly reduce the final deposition footprint of analytes and consequently increase the intensity of SERS signals.

RESULTS/DISCUSSION

Hierarchical plasmonic micro-/nanostructures used in this work consist of Au/Ag nanolaminated plasmonic nanostructures decorated on top of two-tier Si/CNT micro-/nanopillar arrays (Figure 2; CNT, carbon nanotube). Figure 2A illustrates

https://dx.doi.org/10.1021/acsnano.0c04239
ACS Nano 2020, 14, 9521−9531

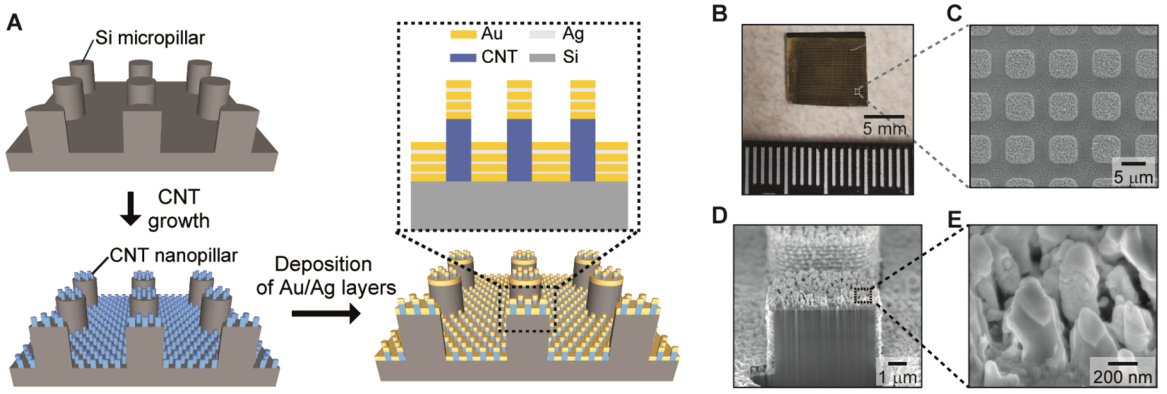

Figure 2. Hierarchical plasmonic micro-/nanostructures. (A) Schematic illustration of the fabrication process to create hierarchical plasmonic micro-/nanostructures. (B) Top-view optical image of the device with hierarchical plasmonic micro-/nanostructures. (C) Top-view and (D, E) cross-sectional SEM images of hierarchical plasmonic micro-/nanostructures.

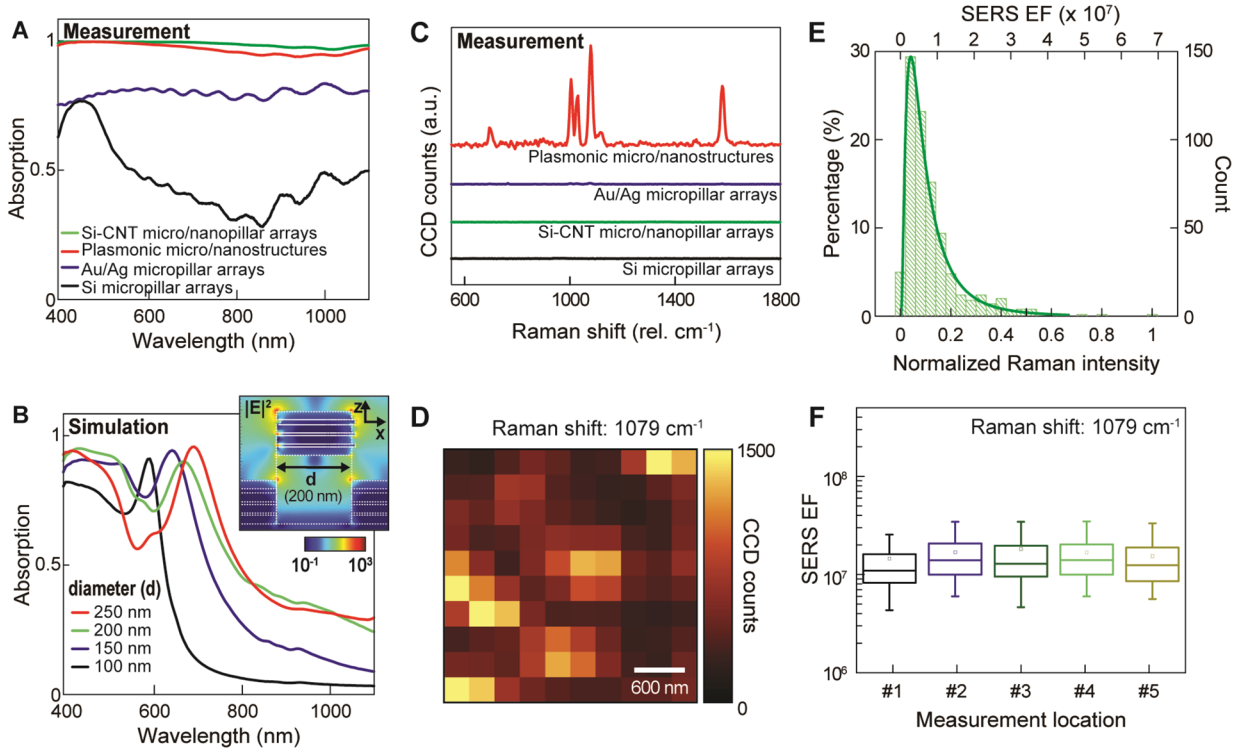

Figure 3. Optical and SERS properties. (A) Measured reflectance spectra of hierarchical plasmonic micro-/nanostructures in comparison with those from reference samples. (B) FDTD-calculated reflectance spectra of plasmonic nanostructures with different nanopillar diameters (d = 100, 150, 200, and 250 nm). Inset: FDTD-calculated x−z distribution map of $|E|^2$ for the plasmonic nanostructure with a nanopillar diameter of 200 nm (d = 200 nm) at its resonant wavelength (λ = 670 nm). (C) Raman spectra of benzenethiol (BZT) from hierarchical plasmonic micro-/nanostructures in comparison with control samples. (D) Confocal Raman images for BZT signals at 1079 cm^{-1} from hierarchical plasmonic micro-/nanostructures. (E) Histogram of Raman signal intensities and the corresponding SERS EFs (1079 cm^{-1}) for hierarchical plasmonic micro-/nanostructures. (F) SERS EFs (1079 cm^{-1}) of the nanolaminated hierarchical SERS substrates at 5 different locations. Boxes were plotted with 1.5 interquartile range (IQR), and lines from top to bottom indicate Q75 + 1.5 IQR, Q75, Q50, Q25, Q25 − 1.5 IQR.

the key steps to fabricate hierarchical plasmonic micro-/nanostructures. As described in our previous work,[33] we created the two-tier Si/CNT micro-/nanopillar arrays by the combination of top-down microfabrication and bottom-up chemical synthesis approaches. Briefly, we fabricated square-shaped Si micropillar arrays by photolithography patterning and deep reactive ion etching. Then, a thin layer of nickel was coated on the microstructured substrate as a catalyst to grow CNTs by plasma-enhanced chemical vapor deposition (PECVD). Finally, we deposited alternating layers of Au (25 nm thick) and Ag (6, 8, and 12 nm thick from the bottom to the top, respectively) on the two-tier Si/CNT micro-/nanopillar array structures by electron-beam evaporation.

As shown in the top-view of optical image (Figure 2B), hierarchical plasmonic micro-/nanostructures have a dark appearance reflecting a broadband absorption in the visible spectrum. From the top-view (Figure 2C) and the cross-sectional view (Figure 2D,E) of scanning electron microscopy (SEM) images, we can observe a good microscale uniformity of hierarchical plasmonic micro-/nanostructures. Here, the Si

https://dx.doi.org/10.1021/acsnano.0c04239
ACS Nano 2020, 14, 9521−9531

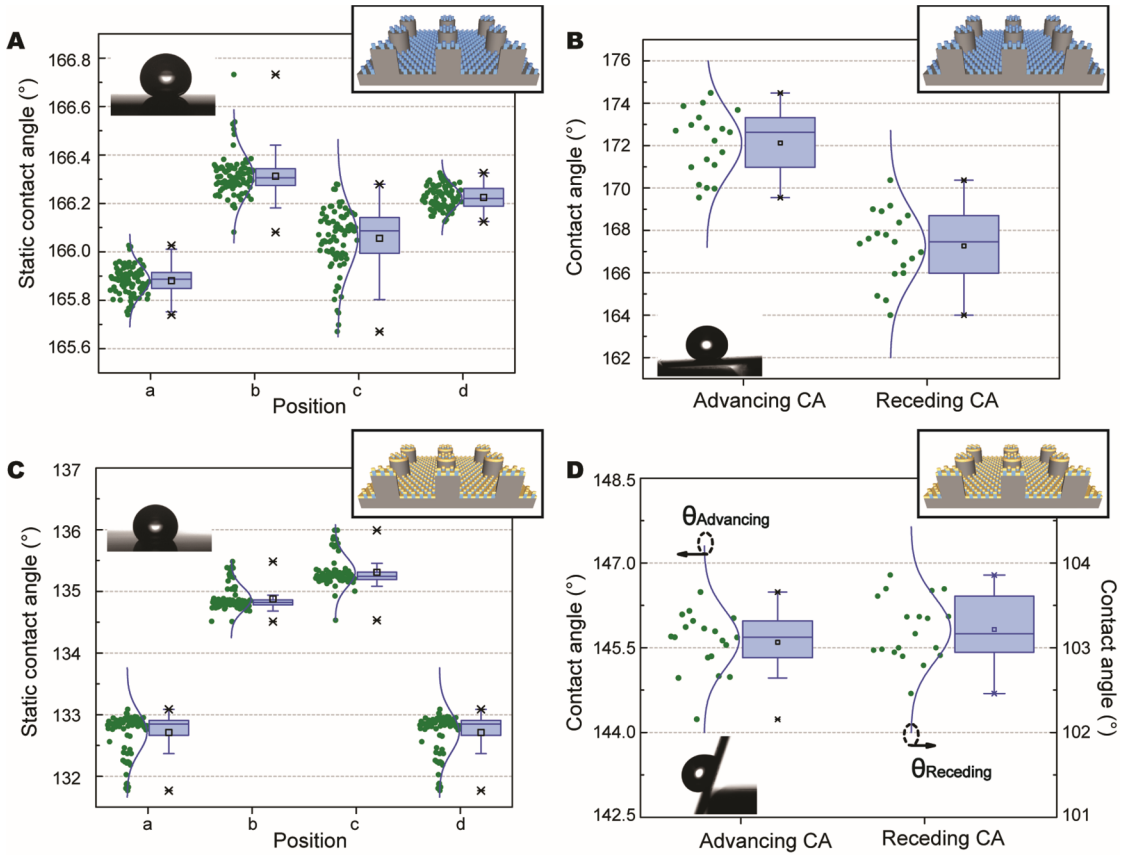

Figure 4. Surface wettability by contact angle measurements. (A) Static and (B) dynamic contact angle measurement results for hierarchical CNT-Si micro-/nanostructures without the nanolaminated deposition of alternating Au and Ag layers. (C) Static and (D) dynamic contact angle measurement results for hierarchical plasmonic micro-/nanostructures with the nanolaminated deposition of alternating Au and Ag layers. The insets of droplets in panels B and D show the sliding angles of droplets on micro-/nanostructured surfaces without and with alternating Au/Ag coatings, respectively.

micropillar arrays have a micropillar width of 6 μm, a micropillar height of 6 μm, and a periodicity of 9 μm. In contrast, the CNT nanopillars with about 30% solid−liquid contact fraction have relatively large variations in both the diameters and heights ranging from 50 to 600 nm, due to the random CNT growth process in PECVD. The line-of-sight electron-beam deposition of alternating Au and Ag layers on top of CNT nanopillars can generate nanolaminated plasmonic nanostructures as optical nanoantennas with intrinsic hot spots that can concentrate light in the nanoscale (Figure 2E).[8]

We carried out broadband absorption measurements to examine the optical properties of the hierarchical plasmonic micro-/nanostructures in comparison with different benchmark or control samples (Figure 3A), including bare Si micropillar arrays, Au/Ag-coated Si micropillar arrays, and two-tier Si-CNT micro-/nanopillar arrays. In the entire visible and near-infrared wavelength range between 400 and 1000 nm, both the hierarchical plasmonic micro-/nanostructures and Si-CNT micro-/nanopillars show flat high absorption spectra over 90%. Despite their similarity in the far-field optical spectra, hierarchical plasmonic micro-/nanostructures can achieve nanolocalized light concentration and induce optical absorption within an ultrathin skin depth (<30 nm) of metal layers.[34] In contrast, the Si-CNT micro-/nanopillars have a much larger light penetration depth due to their smaller free carrier density. As expected, Au/Ag-coated micropillar arrays and Si micropillar arrays show weaker absorption than the hierarchical plasmonic micro-/nanostructures because they lack metal nanostructures to support localized surface plasmon modes.

To understand the microscopic origin of the observed optical properties on the hierarchical plasmonic micro-/nanostructures, we performed 3D finite-difference time-domain (FDTD) calculations using commercial software (FDTD solution, Lumerical Inc.) (see details in the Supporting Information). Figure 3B depicts the calculated absorption spectra of nanolaminated Au/Ag plasmonic nanostructures sitting on CNT nanopillars with different diameter d. As the nanopillar diameter increases from 100 to 150, 200, and 250 nm, a distinct resonant absorption peak red-shifts from 595 to 645, 670, and 695 nm, respectively, while the absorption feature below 530 nm does not change the spectral shape due to the interband electronic transitions in Au. The inset of Figure 3B shows the FDTD-calculated near-field distribution map of $|E|^2$ at the resonant wavelength of 670 nm for the nanolaminated Au/Ag plasmonic nanostructures, which are decorated on CNT nanopillars with d = 200 nm. The FDTD-calculated mode profile reveals an electric dipole nature for the localized plasmon modes in the nanolaminated Au/Ag plasmonic nanostructures. Since the resonant wavelengths of electric dipolar plasmon modes strongly depend on the diameters of plasmonic nanostructures, hierarchical plasmonic micro-/nanostructures composed of various plasmonic nanostructures with different diameters can show a broadband

https://dx.doi.org/10.1021/acsnano.0c04239
ACS Nano 2020, 14, 9521−9531

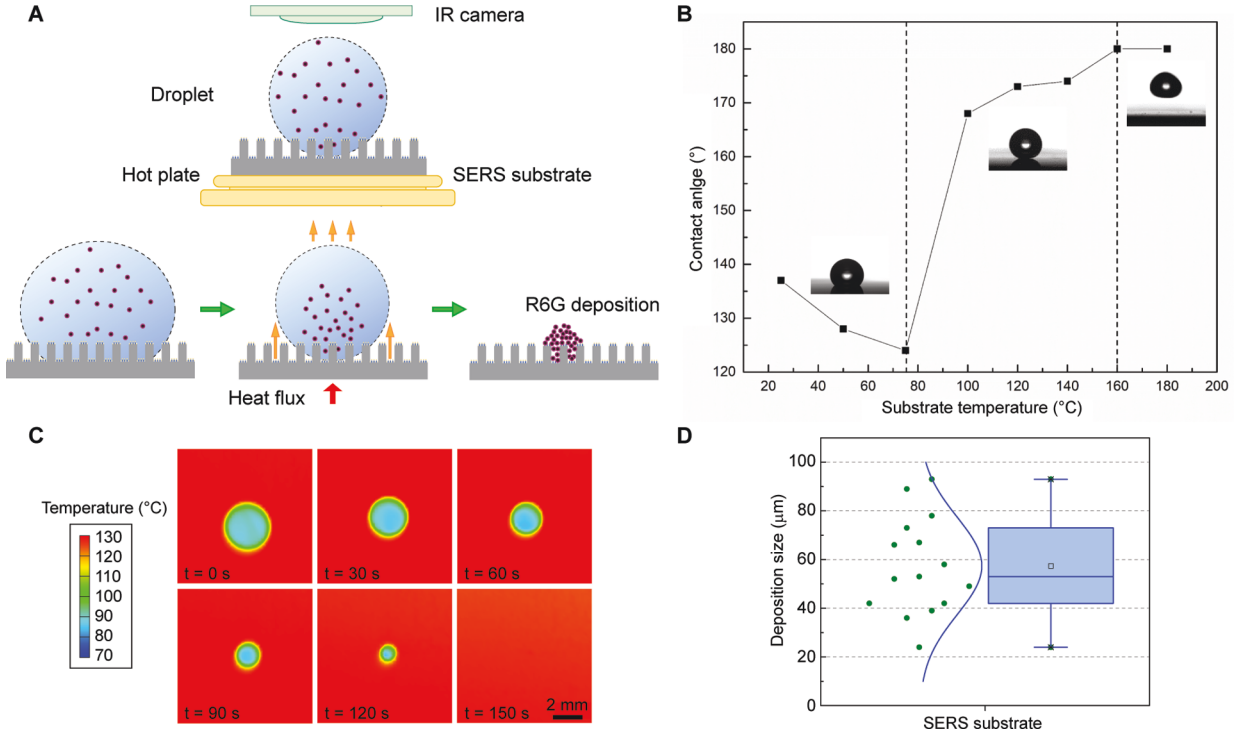

Figure 5. Partial Leidenfrost evaporation of analyte droplets on hierarchical plasmonic micro-/nanostructures. (A) Schematic of the experimental procedure for heat-assisted evaporation of liquid droplets containing R6G molecules. (B) Static contact angle measurements of DI water droplets at different substrate temperatures on hierarchical plasmonic micro-/nanostructures. (C) IR camera images showing the droplet footprint evolution during the evaporation process on the substrate at 130 °C. (D) Deposition repeatability tests of 20 μL R6G water droplets by partial Leidenfrost-assisted evaporation.

optical absorption due to the inhomogeneous broadening effects.[8] Besides, near-field optical simulations show that plasmonic nanostructures can enhance the local electric field intensity $|E|^2$ by up to 3 orders of magnitude, which corresponds to SERS EFs on the order of $\sim 10^6$ according to the $|E|^4$ approximation.[35] Therefore, our numerical calculations predict that hierarchical plasmonic micro-/nanostructures can support SERS hot spots with a broad spectral response.

By Raman measurements of benzenethiol (BZT) molecules assembled on these substrates, we characterized the SERS performance of hierarchical plasmonic micro-/nanostructures in comparison with different benchmark samples (Figure 3C), including bare Si micropillar arrays, Au/Ag-coated micropillar arrays, and two-tier Si-CNT micro-/nanopillar arrays. Figure 3C depicts the average BZT Raman spectra from above-mentioned samples, which were acquired by measuring 10 × 10 pixels over a 3 μm × 3 μm area using a 100 times objective lens (numerical aperture, NA: 0.9) under the excitation of a 785 nm diode laser with 1 mW power by an integration time of 1 s for each pixel. As expected, hierarchical plasmonic micro-/nanostructures exhibit an excellent SERS performance by presenting distinct BZT Raman features. In contrast, the control samples of bare Si micropillar arrays, Au/Ag-coated micropillar arrays, and two-tier Si-CNT micro-/nanopillar arrays did not show any BZT Raman signatures due to the lack of plasmonic nanostructures enhancing local optical fields. From hierarchical plasmonic micro-/nanostructures, five notable Raman peaks of BZT molecules can be observed corresponding to the CS stretching and CCC ring in-plane deformation vibration (at 427 cm^{-1}), the CCC ring in-plane bending mode (at 1004 cm^{-1}), the CH in-plane bending mode (at 1030 cm^{-1}), the CCC ring in-plane breathing mode with CS stretching mode (at 1079 cm^{-1}), and the CC stretching mode (at 1579 cm^{-1}).[36]

By two-dimensional (2D) Raman mapping of the top micropillar regions over multiple positions (Figure 3D), we have evaluated the uniformity of the SERS hot spots on hierarchical plasmonic micro-/nanostructures. As shown in Figure 3E, the histogram of Raman intensities and the corresponding SERS EFs at 1079 cm^{-1} from 5 different regions (500 pixels in total) follow a log-normal distribution curve, reflecting the major SERS contribution from uniformly distributed hot spots instead of a few of individual ones. We used the following definition for the calculation of SERS EFs: $EF = (I_{SERS}/N_{SERS})/(I_{Raman}/N_{Raman})$,[6] where I_{SERS}, I_{Raman}, N_{SERS}, and N_{Raman} are the BZT SERS intensity, neat BZT Raman intensity, the number of BZT molecules contributing to SERS, and the number of BZT molecules contributing to the Raman signal, respectively. Figure 3F illustrates the measured SERS EFs of the hierarchical plasmonic micro-/nanostructures at five different positions with the averaged SERS EFs of 1.45 × 10^7, 1.68 × 10^7, 1.81 × 10^7, 1.67 × 10^7, and 1.53 × 10^7, respectively. The small variations of SERS EFs on these different positions reflect the uniform SERS performance of the scalable and hierarchical plasmonic nanolaminated surfaces for practical SERS applications.

While the magnitude of SERS EFs at hot spots is mainly determined by the optical properties of hierarchical plasmonic micro-/nanostructures, their surface wettability properties also play a vital role in SERS detection performance by influencing the evaporation process of analyte droplets and hence the concentration of dilute analytes thereon. To investigate the surface wettability properties, we used the optical tensiometer (Attension Theta, Biolin Scientific) to measure both the static

https://dx.doi.org/10.1021/acsnano.0c04239
ACS Nano 2020, 14, 9521−9531

and dynamic contact angles (CAs) of water droplets on the samples of hierarchical Si-CNT micro-/nanostructures without nanolaminated Au−Ag deposition (Figure 4A,B) as well as those with nanolaminated Au−Ag deposition (Figure 4C,D). In static CA measurements, we randomly selected 4 positions on each substrate surface to measure the static CA of water droplets of 20 μL and conducted 40 times measurements at each position for statistical analyses (Figure 4A,C). The dynamic CA of each substrate was also measured by dripping a water microdroplet on the surface and then gradually tilting the substrate until the droplet started sliding on it. In total, the advancing CA ($\theta_{advancing}$) and receding CA ($\theta_{receding}$) on each sample were measured 20 times, respectively (Figure 4B,D). Since the standard deviations of both the static and dynamic CA measurements are less than 0.3° according to the statistical analyses (Figure 4A−D), both the samples of hierarchical Si-CNT micro-/nanostructures (Figure 4A,B) and the hierarchical plasmonic micro-/nanostructures (Figure 4C,D) exhibit uniform surface wettabilities.

As shown in Figure 4A,B, the hierarchical Si-CNT micro-/nanostructures without nanolaminated Au−Ag coating show an average static CA of ∼166° (Figure 4A) and a contact angle hysteresis (CAH = $\theta_{advancing} - \theta_{receding}$) of ∼5° (Figure 4B). These results reveal that the hierarchical Si-CNT micro-/nanostructures possess intrinsic superhydrophobicity with a water droplet in the Cassie state on it.[37] In contrast, with nanolaminated Au−Ag coating, hierarchical plasmonic micro-/nanostructures show a reduced static CA of ∼134° (Figure 4C) and an increased CAH of ∼32° (Figure 4D), which reflects a decreased surface hydrophobicity with the water droplet in the Wenzel state[37] due to the deposition of the hydrophilic Au−Ag metal films on top of Si-CNT micro-/nanostructures. To simultaneously accomplish ultrafast and ultrasensitive SERS detection of low-concentration analytes in solutions, we have innovated a surface heating-assisted approach to minimize the analyte deposition footprint *via* carefully controlling the evaporation process of analyte droplets especially on the hierarchical plasmonic micro-/nanostructures. During such a process, only the circumferential base of the evaporating droplet would be ideally levitated to the Cassie state so that its three-phase contact zone can continuously recede without being pinned on the rough surface.[37] Contrary to this, a water droplet during natural evaporation, *i.e.*, without surface heating, on the hierarchical plasmonic micro-/nanostructures is entirely in the Wenzel state as reflected in Figure 4C,D; consequently, the pinning effect along the contact line of the droplet leads to the final deposition area of similar size to its initial base area (∼1.5 mm in diameter for a 20 μL droplet).

To reduce the final deposition area of dilute analytes contained in a water droplet, which is initially in the Wenzel state on the hierarchical plasmonic micro-/nanostructures, we exploited the Leidenfrost effect to only convert the perimetric rim of the droplet base into the Cassie state by scrutinizingly controlling the substrate heating as illustrated in Figure 5A. Importantly, maintaining a droplet in the Cassie−Wenzel hybrid state, *i.e.*, a Janus droplet, is beneficial for the enrichment of dilute analytes in ultrasensitive SERS detection by (1) providing the depinning mechanism by switching only the bottom circumference of the droplet to the Cassie state so that the evaporating droplet can gradually recede toward the center of the droplet base, *i.e.*, deposition area; and (2) providing the pining force by consecutively holding the bottom center of the droplet in the Wenzel state to avoid the uncontrollable dislodgement of the shrinking droplet for precise deposition of analytes. Additionally, minimizing the Leidenfrost temperature is indispensable to sensing high-temperature-intolerant substances by SERS. Previous studies have found that depending on the surface wettability flat smooth substrates have a pretty high Leidenfrost temperature ranging between 210 and 320 °C for water at atmospheric pressure,[30,38−43] while micro-/nanostructured surfaces of the same materials can lead to over 100 °C reduction of the Leidenfrost temperature.[44−48] In general, to achieve Leidenfrost evaporation of water droplets at moderate heating temperature, the ideal SERS substrates should have (1) micro-/nanostructured roughness with a large surface-to-volume ratio and proper wettability for easy generation of the self-evaporated vapor layer as a thermal barrier; and (2) high thermal conductivity for well-controlled interfacial heating and droplet evaporation. Some studies have shown good SERS performance on microarrays of plasmonic nanostructures formed on hydrophobic polydimethylsiloxane (PDMS) substrates. However, PDMS is not a suitable substrate material for Leidenfrost evaporation due to its poor thermal conductivity.[49−51] As such, our SERS substrates based on Si-CNT hierarchical plasmonic micro-/nanostructures satisfy the above two requirements. The conventional Leidenfrost effect can induce the Wenzel-to-Cassie transition on the engineered surfaces in two steps. First, substrate heating incurs evaporation of the liquid within the surface roughness or cavities under the droplet base. Second, the fast-evaporated vapor can fully lift the droplet to the Cassie state.[52] By precisely controlling the substrate heating temperature, however, it is amazingly possible to maintain the droplet in the Cassie−Wenzel Janus state,[53] which means only the circumferential contact zone is levitated to the Cassie state while the central contact base remains pinned in the Wenzel state throughout the continuous receding of the peripheral zone toward the base center, *i.e.*, partial Leidenfrost evaporation.

To investigate the effects of substrate heating on the droplet wetting transition between the Wenzel state and the Cassie state, we measured the contact angle evolution of deionized (DI) water droplets of 20 μL under various substrate temperatures ranging from 25 to 185 °C (Figure 5B). According to the measurements, a water droplet on a hot hierarchical plasmonic micro-/nanostructured surface can experience three different phases. In the first phase, when the substrate temperature T increases from 25 to 75 °C, the droplet stays in the Wenzel state, and its contact angle decreases from ∼138° to ∼123° due to the reduced surface tension of water. During the second phase, when T increases from 75 to 160 °C, the droplet experiences the transition from the Wenzel state to the Cassie−Wenzel hybrid state; thus, the droplet contact angle dramatically increases from ∼123° to ∼180° with the continuously shrinking contact area due to the levitating force of vapor. During the third phase, when T rises from 160 to 185 °C, the droplet is completely levitated with no contact with the substrate due to the (conventional) Leidenfrost effect. To minimize the deposition footprint size of the analyte molecules at a prescribed spot, keeping the droplet in the second phase, *i.e.*, partial Leidenfrost evaporation, is highly preferred.

We dripped an analyte droplet of 20 μL on the hierarchical plasmonic micro-/nanostructured surface under the room

https://dx.doi.org/10.1021/acsnano.0c04239
ACS Nano 2020, 14, 9521−9531

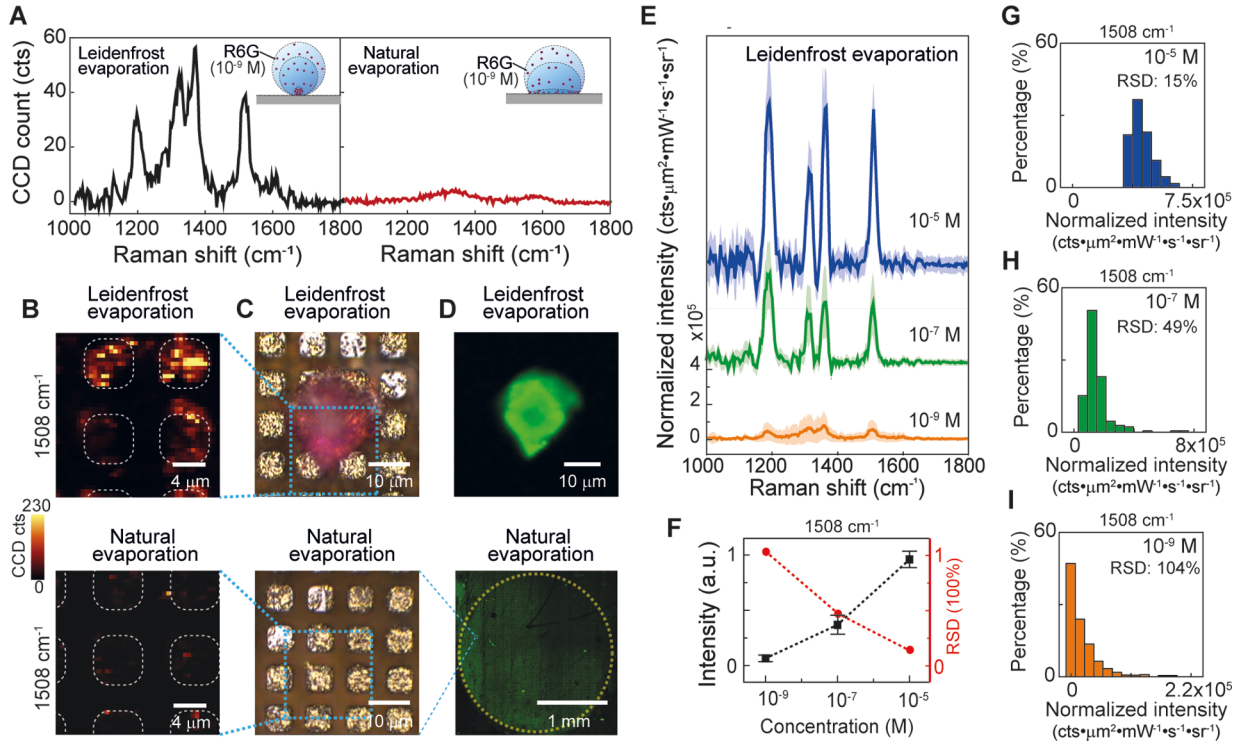

Figure 6. Partial Leidenfrost evaporation-assisted SERS detection of concentrated R6G molecules. (A) Raman spectra of R6G molecules deposited on hierarchical plasmonic micro-/nanostructures *via* the partial Leidenfrost evaporation of 20 μL R6G (10^{-9} M) water droplets with substrate heating (left) or natural droplet evaporation without substrate heating (right). (B) Confocal Raman images, (C) bright-field images, and (D) fluorescence images of R6G molecules deposited on hierarchical plasmonic micro-/nanostructures *via* the partial Leidenfrost droplet evaporation with substrate heating (top) or natural droplet evaporation without substrate heating (bottom). (E) Raman spectra with standard deviations (shaded regions) of the deposited R6G molecules *via* the partial Leidenfrost evaporation of 20 μL R6G water droplets at different concentrations of 10^{-5}, 10^{-7}, and 10^{-9} M. (F) Dependence of R6G Raman signal intensities (1508 cm^{-1}) and relative standard deviation (RSD) values on the R6G concentrations of analyte droplets in partial Leidenfrost evaporation-assisted SERS measurements. Histograms of R6G Raman signal intensities at different R6G concentrations of (G) 10^{-5} M, (H) 10^{-7} M, and (I) 10^{-9} M.

temperature condition ($T_{ambient}$ = 20 °C). To maintain the droplet in the Cassie–Wenzel hybrid state with a stable evaporation rate, we set the initial substrate temperature at 130 °C on a hot plate and then let it naturally cool down by turning off the hot plate. Figure 5C shows the dynamic evolution of the temperature contour of a droplet in the Cassie–Wenzel hybrid state during partial Leidenfrost evaporation, recorded by an IR camera (A300, FLIR Systems) (Figures S2–S4, Supporting Information). The whole evaporation process lasted only ~150 s, and the temperature of the droplet center during the overall evaporation process was amazingly maintained below 90 °C according to the IR camera images (Figure 5C). Thus, the current heating approach to inducing partial Leidenfrost evaporation is compatible with the SERS detection of analyte substances with chemical stability or biocompatibility under 90 °C. To evaluate the repeatability of the partial Leidenfrost-assisted deposition, we performed 15 trials of partial Leidenfrost tests of 20 μL Rhodamine 6G (R6G) water droplets using the same heating approach. The statistical results show that the mean deposition footprint is about 57.4 μm in diameter, with a standard deviation of 20.0 μm (Figure 5D). For Leidenfrost-assisted SERS detection of temperature-sensitive analyte molecules (such as proteins and DNAs), it is essential to further reduce the Leidenfrost temperature, which can be achieved by (1) increasing the filling ratio of air entrapped in the micropillar forest, (2) reducing the surface energy of micropillars, or (3) reducing the surrounding pressure during the evaporation process,[30,39,54] *i.e.*, in a vacuum chamber.

Compared to natural evaporation, partial Leidenfrost-assisted evaporation of droplets in the hybrid Janus state can lead to a much smaller analyte deposition area on hierarchical plasmonic micro-/nanostructures. To experimentally demonstrate the effectiveness of partial Leidenfrost evaporation-assisted ultrasensitive SERS detection, we conducted a side-by-side evaluation between partial Leidenfrost and natural evaporation processes in SERS measurements of 20 μL R6G water droplets at a low concentration of 10^{-9} M. Figure 6A depicts the average Raman spectra at the R6G deposition areas on hierarchical plasmonic micro-/nanostructures after the partial Leidenfrost evaporation and natural evaporation, respectively. We acquired the average Raman spectra by measuring 40 × 40 pixels over a 20 μm × 20 μm area (laser wavelength, 785 nm; laser power, 1.3 mW; integration time, 0.1 s/pixel) using a 100 times objective lens (NA: 0.9) with the focus on the top surface of the micropillar structures. As shown in Figure 6A, partial Leidenfrost evaporation of the R6G droplets in the hybrid Janus state allows direct SERS detection of R6G at a concentration as low as 10^{-9} M, while we cannot observe any R6G Raman signatures through the natural evaporation process. Accordingly, the 2D confocal Raman image shows intense R6G SERS spatial distribution patterns at 1508 cm^{-1} on the top surface (tips) of hierarchical plasmonic micro-/nanostructures from partial Leidenfrost evaporation (Figure 6B, top), but not from natural evaporation (Figure 6B,

https://dx.doi.org/10.1021/acsnano.0c04239
ACS Nano 2020, 14, 9521–9531

bottom). As expected, strong R6G SERS signals were also detected on the bottom plane (cavities) of the hierarchical plasmonic micro-/nanostructures following partial Leidenfrost evaporation (Figure S5, Supporting Information), which confirms that the droplet stayed in the hybrid Cassie−Wenzel Janus state with the final analyte deposition footprint formed both on top of the micropillars and in the micropillar cavities of the hierarchical SERS substrate. Figure 6C,D shows the bright-field images and the fluorescence images of the R6G deposited areas on hierarchical plasmonic micro-/nanostructures following partial Leidenfrost evaporation (Figure S6, Supporting Information) and natural evaporation, respectively. By partial Leidenfrost evaporation, the bright-field image (Figure 6C, top) clearly shows a red circular-shaped pattern of densely packed R6G molecules with a final deposition area of ~450 μm^2 (deposition size ~24 μm), and its shape is in good agreement with the R6G pattern measured by Raman imaging (Figure 6B, top) and fluorescence imaging (Figure 6D, top) at the same region of the sample. The excellent shape consistency for the final R6G deposition area between the Raman image, the bright-field image, and the fluorescence image reflects the well-controlled SERS protocols without any contaminants introduced on the SERS surface during the partial Leidenfrost evaporation of the low-concentration R6G droplets.

In contrast to the several minutes of partial Leidenfrost evaporation, natural evaporation of the same-sized droplets of R6G solutions (20 μL, 10^{-9} M) on the hierarchical plasmonic micro-/nanostructures at room temperature took a much longer time of ~1.5 h. Natural evaporation also resulted in a much larger final R6G deposition footprint (~2 × 2 mm^2), as illustrated in the fluorescence image (Figure 6D, bottom). Therefore, compared to natural evaporation, partial Leidenfrost evaporation of analyte droplets can effectively reduce the final analyte deposition area and accordingly increase the density of analyte molecules by a factor of 10^3−10^4 in hot spots of hierarchical plasmonic micro-/nanostructures without the need for any extra hydrophobic coating. As expected, we are not able to detect any R6G Raman signals from the hierarchical plasmonic micro-/nanostructures after natural evaporation due to the sparse surface density of R6G (Figure 6A, right). The 2D SERS image (Figure 6B, bottom) shows a few pixels with some weak intensities due to the broad background emission from the substrate instead of Raman scattering from R6G molecules (Figure 6A, right, and Figure S7 in the Supporting Information). The measured SERS signal intensity depends on not only the concentration of R6G in the droplet and SERS EFs of hot spots but also the experimental conditions. To allow a quantitative comparison of SERS signal intensity at different R6G concentrations between measurements, we conducted a normalization process to remove the contributions from different experimental conditions. Figure 6E depicts normalized SERS spectra with standard deviations (shaded regions) under 785 nm laser excitation for analyte water droplets at different R6G concentrations ranging from 10^{-5} to 10^{-9} M, which were measured by 2D Raman mapping over 20 × 20 pixels at the R6G deposition positions on the hierarchical plasmonic micro-/nanostructures after partial Leidenfrost evaporation. The normalized SERS signal intensity has a unit of cts μm^2 mW^{-1} s^{-1} sr^{-1} by considering the excitation laser power, the deposition area of the R6G droplet, the integration time, and the solid angle of the collection lens. The different background noise levels in the normalized spectra at different R6G concentrations are mainly due to the different normalization factors between the measurements. As the R6G concentration increases from 10^{-9} to 10^{-7} and 10^{-5} M, the relative Raman peak intensities at 1508 cm^{-1} increase from ~6% to ~37% and ~100% (Figure 6F), respectively, showing a roughly linear response similar to previous observations.[17] In contrast, the relative standard deviations (RSDs) of Raman signals decrease from 104% to 49% and 15% with increasing R6G concentrations from 10^{-9} to 10^{-7} and 10^{-5} M (Figure 6F), which reflects a decreasingly stochastic nature for the random deposition of higher-density analyte molecules into discrete SERS hot spots. To investigate the dependence of SERS signal uniformity among different pixels on the analyte concentration, we plotted the histograms of 1508 cm^{-1} Raman signal intensities at different R6G concentrations (Figure 6G−I). As the R6G concentration decreases from 10^{-5} to 10^{-9} M, the histogram profiles evolve from a log-normal shape to a power-law shape due to the increased portion of low-signal pixels among total pixels. The above concentration-dependent studies demonstrate that partial Leidenfrost evaporation-assisted SERS measurements on hierarchical plasmonic micro-/nanostructures have the potential for fast detection and quantitative analyses of low-concentration analytes in aqueous solutions. By optimizing the hierarchical micro-/nanostructures and meticulously controlling the substrate heating−cooling dynamics,[55] it is possible to further decrease the deposition area of low-concentration analyte droplets *via* partial Leidenfrost evaporation and therefore achieve even higher EFs of SERS detection.

CONCLUSIONS

In conclusion, we have demonstrated a strategy for fast and ultrasensitive SERS detection based on the partial Leidenfrost evaporation of nanomolar analyte droplets on hierarchical plasmonic micro-/nanostructures, which can quickly increase the analyte concentration within a significantly reduced deposition area. Hierarchical plasmonic micro-/nanostructures not only support hot spots with SERS EFs as high as 1.8 × 10^7 but also allow for partial Leidenfrost evaporation at a much lower heating temperature than that on the flat substrates. Compared to natural evaporation, partial Leidenfrost-assisted droplet evaporation can efficiently facilitate the analyte concentration process from hours to several minutes, reduce the final analyte deposition footprint within hundreds of μm^2, and accordingly increase analyte density on hot spots by 3−4 orders of magnitude. Therefore, partial Leidenfrost-assisted SERS on hierarchical plasmonic micro-/nanostructures provides an agile and facile avenue to overcome the diffusion limit for fast and ultrasensitive detection of low-concentration analyte droplets without further chemical treatments on engineered SERS surfaces.

METHODS/EXPERIMENTAL

Hierarchical Surface Fabrication. On a 2 cm × 2 cm Si substrate of 500 μm thickness, squarely positioned micropillars were formed by deep reactive ion etching. The etched Si substrates were coated with a thin layer of nickel as a catalyst, and CNTs were subsequently grown on it by plasma-enhanced chemical vapor deposition. The micropillars are 5 μm in width, 6 μm in height, and spaced 9 μm center to center. The CNT nanopillars are approximately 0.4 μm tall with a 25−30% surface coverage. Lastly, electron-beam deposition was used to deposit alternating layers of Au and Ag (a total of 7 layers and a total thickness of 126 nm) on the hierarchical Si/CNT structures and create multilayered plasmonic nanoantennas. The thickness of the Au layers is 35 nm. For the Ag

https://dx.doi.org/10.1021/acsnano.0c04239
ACS Nano 2020, 14, 9521−9531

layers, 6, 8, and 12 nm were sequentially deposited from bottom to top.

SERS Measurement. For measuring the SERS signals on the nanolaminated hierarchical SERS substrate, benzenethiol (BZT) (CAS: 108-98-5, Sigma-Aldrich) was used as a benchmark analyte. To form a self-assembled monolayer (SAM) of BZT on the substrate, we incubated the substrate in 1 mM ethanol solution for 18 h, cleaned it with a stream of ethanol solution, and dried it with a gentle nitrogen stream. For Raman measurements, we used a confocal Raman microscopy system (Alpha 300rsa+, WITec). By using a collimator, beam splitter, and long-pass filter for 785 nm, we introduced the incident laser and collected backscattered signals simultaneously. The laser power was 1 mW, and the integration time was 1 s per pixel. For the Raman measurement of Rhodamine 6G (R6G) (CAS: 989-38-8, Sigma-Aldrich), the laser power was 1.3 mW, and the integration time was 0.1 s per pixel.

ASSOCIATED CONTENT

Supporting Information

The Supporting Information is available free of charge at https://pubs.acs.org/doi/10.1021/acsnano.0c04239.

Finite-difference time-domain (FDTD) simulation conditions, energy analysis of wetting transition during the heating-assisted droplet evaporation, IR camera calibration method, confocal Raman image of R6G, fluorescence spectrum, R6G Raman peak origins, R6G Raman spectra from the natural evaporation process, and SERS EF calculation method (PDF)

AUTHOR INFORMATION

Corresponding Authors

Jiangtao Cheng − *Department of Mechanical Engineering, Virginia Tech, Blacksburg, Virginia 24061, United States;* orcid.org/0000-0002-0897-3937; Email: chengjt@vt.edu

Wei Zhou − *Department of Electrical and Computer Engineering, Virginia Tech, Blacksburg, Virginia 24061, United States;* orcid.org/0000-0002-5257-3885; Email: wzh@vt.edu

Authors

Junyeob Song − *Department of Electrical and Computer Engineering, Virginia Tech, Blacksburg, Virginia 24061, United States;* orcid.org/0000-0001-6369-823X

Weifeng Cheng − *Department of Mechanical Engineering, Virginia Tech, Blacksburg, Virginia 24061, United States*

Meitong Nie − *Department of Electrical and Computer Engineering, Virginia Tech, Blacksburg, Virginia 24061, United States*

Xukun He − *Department of Mechanical Engineering, Virginia Tech, Blacksburg, Virginia 24061, United States*

Wonil Nam − *Department of Electrical and Computer Engineering, Virginia Tech, Blacksburg, Virginia 24061, United States;* orcid.org/0000-0002-7804-3049

Complete contact information is available at: https://pubs.acs.org/10.1021/acsnano.0c04239

Author Contributions

§J.S. and W.C. are cofirst authors with equal contribution to this work. W.Z. and J.C. conceived the initial idea for this research and guided the work. J.S., W.C., and X.H. fabricated the experimental samples. J.S., W.C., and M.N. carried out the SERS experiments. J.S., W.C., M.N., W.N., and X.H. analyzed the data. W.N. performed fluorescence imaging. All the authors were responsible for writing the paper and have approved the final version of this manuscript.

Notes

The authors declare no competing financial interest.

ACKNOWLEDGMENTS

J.C. gratefully acknowledges funding support from the U.S. National Science Foundation (NSF) under Awards ECCS 1808931 and CBET 1550299. W.Z. gratefully acknowledges funding support from the Air Force Office of Scientific Research (AFOSR) Young Investigator Award FA9550-18-1-0328 and National Institute of Standards and Technology (NIST) grant 70NANB18H201.

REFERENCES

(1) Fleischmann, M.; Hendra, P. J.; Mcquillan, A. J. Raman-Spectra of Pyridine Adsorbed at a Silver Electrode. *Chem. Phys. Lett.* **1974**, *26*, 163−166.

(2) Jeanmaire, D. L.; Van Duyne, R. P. Surface Raman Spectroelectrochemistry. *J. Electroanal. Chem. Interfacial Electrochem.* **1977**, *84*, 1−20.

(3) Halvorson, R. A.; Vikesland, P. J. Surface-Enhanced Raman Spectroscopy (SERS) for Environmental Analyses. *Environ. Sci. Technol.* **2010**, *44*, 7749−7755.

(4) Le Ru, E. C.; Blackie, E.; Meyer, M.; Etchegoin, P. G. Surface Enhanced Raman Scattering Enhancement Factors: A Comprehensive Study. *J. Phys. Chem. C* **2007**, *111*, 13794−13803.

(5) Etchegoin, P. G.; Le Ru, E. C. A Perspective on Single Molecule SERS: Current Status and Future Challenges. *Phys. Chem. Chem. Phys.* **2008**, *10*, 6079−6089.

(6) Song, J.; Nam, W.; Zhou, W. Scalable High-Performance Nanolaminated SERS Substrates Based on Multistack Vertically Oriented Plasmonic Nanogaps. *Adv. Mater. Technol.* **2019**, *4*, 1800689.

(7) Halas, N. J.; Lal, S.; Chang, W. S.; Link, S.; Nordlander, P. Plasmons in Strongly Coupled Metallic Nanostructures. *Chem. Rev.* **2011**, *111*, 3913−3961.

(8) Song, J.; Zhou, W. Multiresonant Composite Optical Nanoantennas by Out-Of-Plane Plasmonic Engineering. *Nano Lett.* **2018**, *18*, 4409−4416.

(9) Jiang, J.; Bosnick, K.; Maillard, M.; Brus, L. Single Molecule Raman Spectroscopy at the Junctions of Large Ag Nanocrystals. *J. Phys. Chem. B* **2003**, *107*, 9964−9972.

(10) Craig, A. P.; Franca, A. S.; Irudayaraj, J. Surface-Enhanced Raman Spectroscopy Applied to Food Safety. *Annu. Rev. Food Sci. Technol.* **2013**, *4*, 369−380.

(11) Zheng, X. S.; Jahn, I. J.; Weber, K.; Cialla-May, D.; Popp, J. Label-Free SERS in Biological and Biomedical Applications: Recent Progress, Current Challenges and Opportunities. *Spectrochim. Acta, Part A* **2018**, *197*, 56−77.

(12) Zong, C.; Xu, M.; Xu, L.-J.; Wei, T.; Ma, X.; Zheng, X.-S.; Hu, R.; Ren, B. Surface-Enhanced Raman Spectroscopy for Bioanalysis: Reliability and Challenges. *Chem. Rev.* **2018**, *118*, 4946−4980.

(13) Sheehan, P. E.; Whitman, L. J. Detection Limits for Nanoscale Biosensors. *Nano Lett.* **2005**, *5*, 803−807.

(14) Nair, P. R.; Alam, M. A. Performance Limits of Nanobiosensors. *Appl. Phys. Lett.* **2006**, *88*, 233120.

(15) De Angelis, F.; Gentile, F.; Mecarini, F.; Das, G.; Moretti, M.; Candeloro, P.; Coluccio, M. L.; Cojoc, G.; Accardo, A.; Liberale, C.; Zaccaria, R. P.; Perozziello, G.; Tirinato, L.; Toma, A.; Cuda, G.; Cingolani, R.; Di Fabrizio, E. Breaking the Diffusion Limit with Superhydrophobic Delivery of Molecules to Plasmonic Nanofocusing SERS Structures. *Nat. Photonics* **2011**, *5*, 682−687.

(16) Gentile, F.; Das, G.; Coluccio, M. L.; Mecarini, F.; Accardo, A.; Tirinato, L.; Tallerico, R.; Cojoc, G.; Liberale, C.; Candeloro, P.; Decuzzi, P.; De Angelis, F.; Di Fabrizio, E. Ultra Low Concentrated

https://dx.doi.org/10.1021/acsnano.0c04239
ACS Nano 2020, 14, 9521−9531

Molecular Detection Using Super Hydrophobic Surface Based Biophotonic Devices. *Microelectron. Eng.* **2010**, *87*, 798−801.
(17) Lee, H. K.; Lee, Y. H.; Zhang, Q.; Phang, I. Y.; Tan, J. M. R.; Cui, Y.; Ling, X. Y. Superhydrophobic Surface-Enhanced Raman Scattering Platform Fabricated by Assembly of Ag Nanocubes for Trace Molecular Sensing. *ACS Appl. Mater. Interfaces* **2013**, *5*, 11409−11418.
(18) Rui Tan, J. M.; Ruan, J. J.; Lee, H. K.; Phang, I. Y.; Ling, X. Y. A Large-Scale Superhydrophobic Surface-Enhanced Raman Scattering (SERS) Platform Fabricated *via* Capillary Force Lithography and Assembly of Ag Nanocubes for Ultratrace Molecular Sensing. *Phys. Chem. Chem. Phys.* **2014**, *16*, 26983−26990.
(19) Gao, Y. K.; You, T. T.; Yang, N.; Zhang, C. M.; Yin, P. G. Superhydrophobic 3D Forest-Like Ag Microball/Nanodendrite Hierarchical Structure as SERS Sensor for Rapid Droplets Detection. *Adv. Mater. Interfaces* **2019**, *6*, 1801966.
(20) Park, S.-G.; Mun, C.; Xiao, X.; Braun, A.; Kim, S.; Giannini, V.; Maier, S. A.; Kim, D.-H. Surface Energy-Controlled SERS Substrates for Molecular Concentration at Plasmonic Nanogaps. *Adv. Funct. Mater.* **2017**, *27*, 1703376−1703376.
(21) Li, H. Z.; Yang, Q.; Hou, J.; Li, Y. A.; Li, M. Z.; Song, Y. L. Bioinspired Micropatterned Superhydrophilic Au-Areoles for Surface-Enhanced Raman Scattering (SERS) Trace Detection. *Adv. Funct. Mater.* **2018**, *28*, 1800448.
(22) Wu, Y. W.; Hang, T.; Komadina, J.; Ling, H. Q.; Li, M. High-Adhesive Superhydrophobic 3D Nanostructured Silver Films Applied as Sensitive, Long-Lived, Reproducible and Recyclable SERS Substrates. *Nanoscale* **2014**, *6*, 9720−9726.
(23) Yang, S.; Hricko, P. J.; Huang, P. H.; Li, S.; Zhao, Y.; Xie, Y.; Guo, F.; Wang, L.; Huang, T. J. Superhydrophobic Surface Enhanced Raman Scattering Sensing Using Janus Particle Arrays Realized by Site-Specific Electrochemical Growth. *J. Mater. Chem. C* **2014**, *2*, 542−547.
(24) Yan, Z. X.; Zhang, Y. L.; Wang, W.; Fu, X. Y.; Jiang, H. B.; Liu, Y. Q.; Verma, P.; Kawata, S.; Sun, H. B. Superhydrophobic SERS Substrates Based on Silver-Coated Reduced Graphene Oxide Gratings Prepared by Two-Beam Laser Interference. *ACS Appl. Mater. Interfaces* **2015**, *7*, 27059−27065.
(25) He, X.; Liu, Y.; Xue, X.; Liu, J.; Liu, Y.; Li, Z. Ultrasensitive Detection of Explosives: *via* Hydrophobic Condensation Effect on Biomimetic SERS Platforms. *J. Mater. Chem. C* **2017**, *5*, 12384−12392.
(26) Wang, A.; Jiang, L.; Li, X.; Xie, Q.; Li, B.; Wang, Z.; Du, K.; Lu, Y. Low-Adhesive Superhydrophobic Surface-Enhanced Raman Spectroscopy Substrate Fabricated by Femtosecond Laser Ablation for Ultratrace Molecular Detection. *J. Mater. Chem. B* **2017**, *5*, 777−784.
(27) Xu, F. G.; Zhang, Y.; Sun, Y. J.; Shi, Y.; Wen, Z. W.; Li, Z. Silver Nanoparticles Coated Zinc Oxide Nanorods Array as Superhydrophobic Substrate for the Amplified SERS Effect. *J. Phys. Chem. C* **2011**, *115*, 9977−9983.
(28) Liu, H.; Yang, Z.; Meng, L.; Sun, Y.; Wang, J.; Yang, L.; Liu, J.; Tian, Z. Three-Dimensional and Time-Ordered Surface-Enhanced Raman Scattering Hotspot Matrix. *J. Am. Chem. Soc.* **2014**, *136*, 5332−5341.
(29) Yang, S. K.; Dai, X. M.; Stogin, B. B.; Wong, T. S. Ultrasensitive Surface-Enhanced Raman Scattering Detection in Common Fluids. *Proc. Natl. Acad. Sci. U. S. A.* **2016**, *113*, 268−273.
(30) Kim, H.; Truong, B.; Buongiorno, J.; Hu, L. W. On the Effect of Surface Roughness Height, Wettability, and Nanoporosity on Leidenfrost Phenomena. *Appl. Phys. Lett.* **2011**, *98*, 83121.
(31) Zhong, L.; Guo, Z. Effect of Surface Topography and Wettability on the Leidenfrost Effect. *Nanoscale* **2017**, *9*, 6219−6236.
(32) Zhao, L.; Cheng, J. T. The Mechanism and Universal Scaling Law of the Contact Line Friction for the Cassie-State Droplets on Nanostructured Ultrahydrophobic Surfaces. *Nanoscale* **2018**, *10*, 6426−6436.
(33) Cheng, J. T.; Vandadi, A.; Chen, C. L. Condensation Heat Transfer on Two-Tier Superhydrophobic Surfaces. *Appl. Phys. Lett.* **2012**, *101*, 2649−2653.
(34) Barnes, W. L. Surface Plasmon-Polariton Length Scales: A Route to Sub-Wavelength Optics. *J. Opt. A: Pure Appl. Opt.* **2006**, *8*, S87−S93.
(35) Ding, S. Y.; You, E. M.; Tian, Z. Q.; Moskovits, M. Electromagnetic Theories of Surface-Enhanced Raman Spectroscopy. *Chem. Soc. Rev.* **2017**, *46*, 4042−4076.
(36) Joo, T. H.; Kim, M. S.; Kim, K. Surface-Enhanced Raman Scattering of Benzenethiol in Silver Sol. *J. Raman Spectrosc.* **1987**, *18*, 57−60.
(37) Vandadi, A.; Zhao, L.; Cheng, J. T. Resistant Energy Analysis of Self-Pulling Process During Dropwise Condensation on Superhydrophobic Surfaces. *Nanoscale Adv.* **2019**, *1*, 1136−1147.
(38) Tamura, Z.; Tanasawa, Y. Evaporation and Combustion of a Drop Contacting with a Hot Surface. *Symp. (Int.) Combust., [Proc.]* **1958**, *7*, 509−522.
(39) Emmerson, G. S. The Effect of Pressure and Surface Material on the Leidenfrost Point of Discrete Drops of Water. *Int. J. Heat Mass Transfer* **1975**, *18*, 381−386.
(40) Xiong, T. Y.; Yuen, M. C. Evaporation of a Liquid Droplet on a Hot Plate. *Int. J. Heat Mass Transfer* **1991**, *34*, 1881−1894.
(41) Bernardin, J. D.; Mudawar, I. The Leidenfrost Point: Experimental Study and Assessment of Existing Models. *J. Heat Transfer* **1999**, *121*, 894−903.
(42) Liu, G.; Craig, V. S. Macroscopically Flat and Smooth Superhydrophobic Surfaces: Heating Induced Wetting Transitions up to the Leidenfrost Temperature. *Faraday Discuss.* **2010**, *146*, 141−151.
(43) Nagai, N.; Nishio, S. Leidenfrost Temperature on an Extremely Smooth Surface. *Exp. Therm. Fluid Sci.* **1996**, *12*, 373−379.
(44) Kwon, H. M.; Bird, J. C.; Varanasi, K. K. Increasing Leidenfrost Point Using Micro-Nano Hierarchical Surface Structures. *Appl. Phys. Lett.* **2013**, *103*, 201601.
(45) Nair, H.; Staat, H. J.; Tran, T.; van Houselt, A.; Prosperetti, A.; Lohse, D.; Sun, C. The Leidenfrost Temperature Increase for Impacting Droplets on Carbon-Nanofiber Surfaces. *Soft Matter* **2014**, *10*, 2102−2109.
(46) Duursma, G.; Kennedy, R.; Sefiane, K.; Yu, Y. Leidenfrost Droplets on Microstructured Surfaces. *Heat Transfer Eng.* **2016**, *37*, 1190−1200.
(47) Park, I. W.; Fernandino, M.; Dorao, C. A. Effect of Micropillar Characteristics on Leidenfrost Temperature of Impacting Droplets. *Int. Conf. Nanochannels, Microchannels Minichannels, Proc., 14th* **2016**, V001T09A001.
(48) Farokhnia, N.; Sajadi, S. M.; Irajizad, P.; Ghasemi, H. Decoupled Hierarchical Structures for Suppression of Leidenfrost Phenomenon. *Langmuir* **2017**, *33*, 2541−2550.
(49) Chen, Y.; Si, K. J.; Sikdar, D.; Tang, Y.; Premaratne, M.; Cheng, W. Ultrathin Plasmene Nanosheets as Soft and Surface-Attachable SERS Substrates with High Signal Uniformity. *Adv. Opt. Mater.* **2015**, *3*, 919−924.
(50) Si, K. J.; Guo, P.; Shi, Q.; Cheng, W. Self-Assembled Nanocube-Based Plasmene Nanosheets as Soft Surface-Enhanced Raman Scattering Substrates toward Direct Quantitative Drug Identification on Surfaces. *Anal. Chem.* **2015**, *87*, 5263−5269.
(51) Yang, W.; Si, K. J.; Guo, P.; Dong, D.; Sikdar, D.; Premaratne, M.; Cheng, W. Self-Assembled Plasmonic Pyramids from Anisotropic Nanoparticles for High-Efficient SERS. *J. Anal. Test.* **2017**, *1*, 335−343.
(52) Gelderblom, H.; Marin, A. G.; Nair, H.; van Houselt, A.; Lefferts, L.; Snoeijer, J. H.; Lohse, D. How Water Droplets Evaporate on a Superhydrophobic Substrate. *Phys. Rev. E: Stat., Nonlinear, Soft Matter Phys.* **2011**, *83*, 026306.
(53) Tsai, P.; Lammertink, R. G.; Wessling, M.; Lohse, D. Evaporation-Triggered Wetting Transition for Water Droplets upon Hydrophobic Microstructures. *Phys. Rev. Lett.* **2010**, *104*, 116102.
(54) Kruse, C.; Anderson, T.; Wilson, C.; Zuhlke, C.; Alexander, D.; Gogos, G.; Ndao, S. Extraordinary Shifts of the Leidenfrost Temperature from Multiscale Micro/Nanostructured Surfaces. *Langmuir* **2013**, *29*, 9798−9806.

https://dx.doi.org/10.1021/acsnano.0c04239
ACS Nano 2020, 14, 9521−9531

(55) Kano, T.; Isobe, T.; Matsushita, S.; Nakajima, A. Hydrophobicity and Leidenfrost Point of ZnO Nanorod Array Combined with Nanoscale Roughness on the Topmost Surface. *Mater. Chem. Phys.* **2018**, *217*, 192−198.

https://dx.doi.org/10.1021/acsnano.0c04239
ACS Nano 2020, 14, 9521−9531